Drying in Clays: Insights from Within Using X-ray CT

V. N. Georgiannou[1], Ch. Papazoglou[2], and E. M. Pavlopoulou[3]

[1]*Professor, National Technical University of Athens, Athens, Greece, email: vngeor@civil.ntua.gr*

[2]*PhD Candidate, National Technical University of Athens, Athens, Greece, email: c.papazo1994@gmail.com*

[3]*Dr. Civil Engineer, National Technical University of Athens, Athens, Greece, email: epavlop@mail.ntua.gr*

ABSTRACT

X-ray computed tomography (CT), using the recently installed scanner at the National Technical University of Athens (NTUA), provided 3D images at resolutions ranging from 2 to 20 μm, enabling detailed investigation of the internal structure of reconstituted kaolin. Since geomaterials are inherently porous, heterogeneous, and multiphase, the study focuses on quantifying larger macro-porosity features and examining their evolution during one-dimensional loading and subsequent air-drying. Two conditions are considered: (i) a wet phase, in which the samples remain saturated, and (ii) a dry phase, following exposure to atmospheric conditions. The CT observations show that, in the saturated state, the size and volume of larger pores (>20 μm) progressively decrease with increasing vertical stress and become negligible at approximately 1600 kPa. During air-drying, the volume of these macro-pores increases as air invades the pore space, and promotes the formation of desiccation cracks. Despite this increase in macro-porosity, the total volume of the dry samples decreases further relative to their wet counterparts. This additional shrinkage is attributed to contraction of the finer, sub-resolution pore network within the kaolin matrix, which more than compensates for the increase in volume of the larger pores and cracks. At a preload of 50kPa, these CT-resolved macro-porosity features account for approximately 10% of the total pore space, highlighting the importance of interactions across pore scales in governing the volumetric response of fine-grained soils.

Keywords: X-ray micro-computed tomography (μCT); 3D internal structure; multiscale porosity; macro-porosity; reconstituted kaolin; air-drying;

INTRODUCTION

Geomaterials are, by nature porous, multiphase systems whose mechanical behavior is largely controlled by their internal structure. The internal structure is represented by the combination of 'fabric' which describes how particles and pore spaces are arranged, and 'bonding' due to chemical interactions between particles developed after deposition (Mitchell, 1976). Properties such as strength, stiffness, compressibility, and permeability are all directly influenced by soil structure. However, these properties are currently assessed by macroscopic experimental observations. The missing link is direct experimental evidence at the pore scale – evidence that is key to linking microstructural mechanisms to bulk properties.

To assess the bonding effects in natural clays, albeit macroscopically, Burland (1990) suggested to compare their properties to those of the same clay reconstituted in the laboratory. Reconstitution aims to replicate natural sedimentation, while minimising the effects of natural bonding that develop over geological timescales. The reconstituted state therefore provides a controlled reference state against which the enhanced strength, stiffness, and other characteristics of natural clays can be assessed.

However, direct three-dimensional characterisation of clay fabric at this reconstituted reference state, particularly across multiple spatial scales, remains scarce in the literature.

Advanced X-ray CT resolution is typically limited to a few microns and thus can hardly resolve silt or clay particles. As a result previous studies have predominantly applied X-ray CT to coarse-grained soils, where both particles and voids are sufficiently large to be directly imaged (Finno et al., 1997; Riedel et al., 2012; Desrues et al., 2018).

Capturing the fabric of clay whether at platelet scale, and/or platelet formations within aggregates has been a longstanding goal in experimental soil mechanics. Tchalenko (1967) used thin sections to show how, platy kaolinite particles align, and transition from random arrangements in aggregates to preferred orientations under one-dimensional compression and/or shear. Electron Scanning Microscopy (SEM) provides two-dimensional image data at a resolution of 1-10 nm, while Focused Ion Beam–Scanning Electron Microscopy (FIB–SEM) can provide three-dimensional nanoscale information on pores, platelets and aggregates (Zheng & Baudet, 2025; Myouri et al., 2025). However, in these techniques the water within the pore space has to be replaced or removed, and this is a major limitation when studying saturated clays.

To this end, Casarella et al. (2026) employed phase-contrast nano-holo-tomography to obtain unprecedented three-dimensional observations of the microstructural arrangement of clay particles and pore space in fully saturated, one-dimensionally consolidated reconstituted kaolin. Water between individual kaolin platelets was resolved for the first time at a spatial resolution of 50 nm and was classified as micro-porosity, whereas water occupying the larger voids between particle aggregates was classified as macro-porosity. This pore network was characterised within a very small subvolume of the specimen, measuring 108 × 108 × 108 μm³, which, as the authors acknowledge, reflects the necessary trade-off between field of view and spatial resolution at the nanoscale.

However, macro-porosity features change markedly with the scale of observation. For example, when a one-dimensionally consolidated specimen is examined at the microscale rather than the nanoscale, a distinctly heterogeneous structure emerges. Fine-grained soils may contain silt- or sand-sized inclusions and relatively large voids, which are several orders of magnitude larger than the finer pore network within the clay matrix. Xu et al. (2024) prepared reconstituted kaolin samples 32.7 mm in diameter and 4 mm in height by mixing kaolin powder with deionised water to form a slurry at 151% water content. They used X-ray CT to scan the whole sample at a spatial resolution of 20 μm. Their 3D images show a large number of entrained gas bubbles of various shapes, although mostly spherical, and sizes evenly distributed within the saturated kaolin matrix. Larger bubbles, with diameters of up to approximately 500 μm, were used as tracking markers for strain field measurements during drying, hence, their evolution during one-dimensional consolidation following slurry preparation was not investigated, and therefore remains unknown.

Given that reconstitution is a standard preparation method intended to produce homogeneous, saturated clay samples, the presence of these occluded air bubbles within the slurry is an important finding. Their morphology and volume quantification, their pore size distribution, their evolution under mechanical loading, as well as their potential interaction with the finer pore network within the kaolin matrix, therefore warrants further investigation. The authors are not aware of previous studies that have characterised such macro-porosity features in reconstituted clays.

The internal structure of reconstituted kaolin using X-ray computed tomography (CT) is examined in this study. A range of image resolutions from 2 to 20 microns is used to examine consistently the macro-porosity features e.g. pore space within the kaolin matrix and larger pores like bubbles, within the whole sample. Their morphology is extracted using 3D image analysis, their volume is quantified, and their evolution under increasing one dimensional loading in the oedometer is assessed, for fully-saturated reconstituted kaolin samples.

This reference state is subsequently used to quantify changes in the size, shape, and volume of these macro-porosity features induced by air-drying following different levels of preloading.

MATERIAL AND TESTING METHODS

Reconstitution procedure

Kaolin was used in this study; a standard research clay that due to its stable properties, uniformity and commercial availability, has been widely used both in fundamental studies of soil behavior and in physical model tests.

The grading curve of the kaolin is shown in Figure 1 and the properties of the kaolin are included in Table 1. The reconstitution procedure involves mixing the kaolin powder with distilled and deaired water

at a content of 1.2 times its liquid limit (LL=47%) to produce a slurry. The slurry is poured into a metal cylinder of 300 mm diameter where it consolidates one-dimensionally under gradually increasing vertical loads to a stress of 50 kPa. Consolidation is the process by which kaolin compresses under load as pore water slowly drains out. In an oedometer (consolidation cell), the sample can only compress vertically because it is confined in a rigid ring that prevents lateral movement.

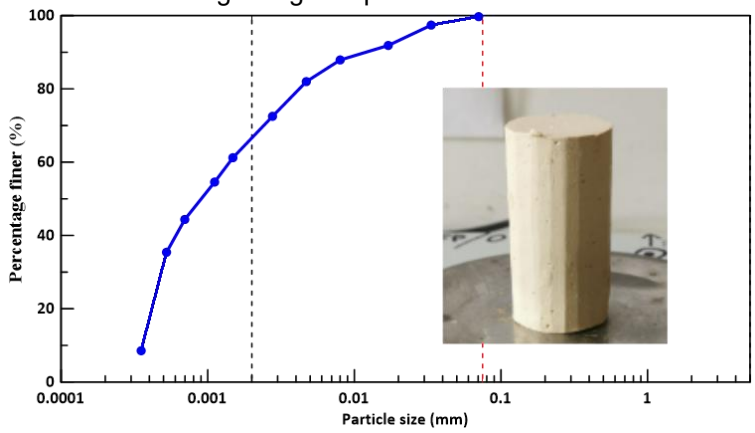

Figure 1. *Grain-size distribution curve*

Table 1. *Properties of kaolin*

	Gs	Liquid Limit (LL) (%)	Plastic Limit (PL) (%)	Plasticity Index (PI) (%)
Kaolin	2.61	47.4	33.5	13.9

At the end of consolidation the sample is unloaded and removed from the metal cylinder. Smaller size samples 50mm in diameter and 19mm in height are trimmed from the big sample and placed in standard oedometers, where they are reloaded to 50 kPa with no additional settlement observed.

In a series of tests, the oedometer specimens were further consolidated to 400, 800, and 1600 kPa, representing the initial vertical effective stresses encountered at different depths in situ. At the end of consolidation each sample is unloaded and subjected to X-ray CT scanning. By preloading the kaolin samples to different stress levels, changes in the internal pore structure can be investigated as the material undergoes progressive compression.

Following unloading, the samples remain saturated under a nominal suction approximately equal in magnitude to the normal stress previously applied in the oedometer. The applied preloading stresses are below the reported air-entry value of kaolin, approximately 2000 kPa (Zhao & Santamarina, 2020; Tsantrizou, 2025), and the specimens therefore remain saturated. The resulting suction preserves, to a first approximation, the mean effective stress established during oedometer loading and consequently helps retain the preload-induced internal structure subsequently captured by X-ray CT.

Following the initial CT scan, the same samples were allowed to air-dry for a couple of days. Subsequent oven-drying produced only a negligible additional change in water content. The air-dried samples were then scanned again using X-ray CT.

Micro-CT scanning: equipment, specifications, image processing procedure

All scans were performed using the RX Solutions EasyTom XL Micro 230 system recently installed in the Soil Mechanics Laboratory at NTUA. The system is a laboratory-based, open-type cone-beam X-ray micro-computed tomography system designed for high-resolution three-dimensional imaging of the internal structure of materials. The scanning parameters were optimized for kaolin to maximize contrast between pore space and solid matrix while minimizing beam-hardening artefacts. The parameters used for all samples are listed in Table 2.

The entire sample was scanned in this study. Figure 2(a) shows a representative greyscale horizontal slice, in which the macro-porosity features, referred to here as ‘bubbles’ for simplicity, appear black.

Figures 2(b) and 2(c) show the corresponding segmented solid phase and the three-dimensional network of macro-porosity features, respectively, for the dry kaolin sample preloaded to 50 kPa.

Three main image-processing steps were used to extract the macro-porosity features, including desiccation cracks in the dry samples, from the three-dimensional greyscale images. First, a median filter with a radius of 2 pixels was applied to reduce image noise while preserving the boundaries of the features of interest, including bubbles and cracks, whose characteristic widths were at least 2 pixels. Second, a variance filter with a radius of 1 pixel was applied to the greyscale image to enhance the boundaries, or shells, of the bubbles and cracks. A threshold value of 72 was then used for binarization, separating the kaolin matrix from these boundaries. Third, a sequence of morphological operations—dilation, hole filling, and erosion—was applied to close the detected shells and generate binary images containing fully segmented bubbles and cracks. Individual features were subsequently identified and assigned unique labels. The three-dimensional reconstructions showed that the bubbles exhibit a range of sizes and shapes. Their geometrical characteristics were quantified from the labelled images, and their volumes and size distributions were calculated using Python scripts incorporating functions from the SPAM library. To distinguish bubbles from desiccation cracks, the true sphericity (Ψ) of each segmented feature was calculated. Features with $\Psi > 0.6$ were classified as bubbles, whereas those with $\Psi \leq 0.6$ were classified as cracks.

Table 2. *Scanning parameters*

Parameter	Value
Tube Voltage	160 kV
Tube Current	119–132 µA
Physical Filter	Aluminum, 0.5 mm
Image Size	2456 × 1944 pixels
Bit Depth (raw)	16 bit
Detector Pixel Size	0.124 mm
Geometry	Cone Beam
Number of Projections	360° rotation

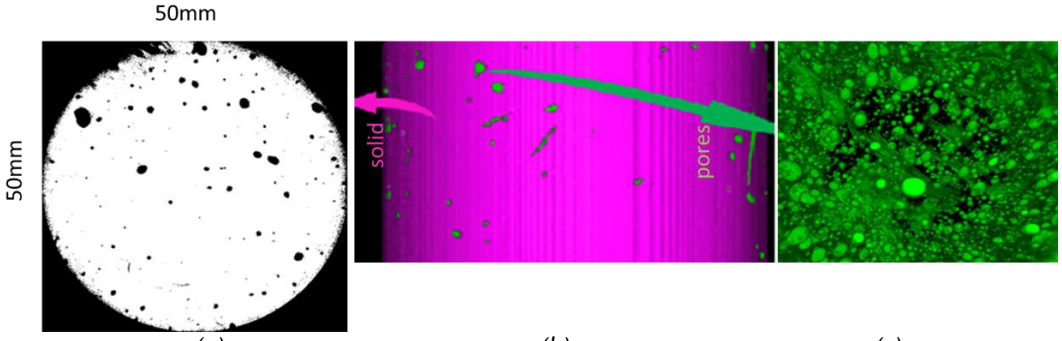

Figure 2. *(a) greyscale horizontal slice; (b) solid phase and (c) pore network of macro-porosity features for the dry kaolin sample preloaded to 50 kPa*

ANALYSIS OF RESULTS

Morphology of pore space

Figures 3(a) and 3(b) show horizontal slices acquired at higher (2µm) and lower (20µm) resolution respectively, for an air-dried kaolin sample preloaded to 50 kPa. Void spaces are shown in black, and in Figure 3(a) pores smaller than approximately 5µm can be seen to be relatively uniformly distributed within the kaolin matrix. Larger silt-sized particles are shown in white, whereas the kaolin matrix, comprising particle aggregates together with interparticle voids and/or retained water, appears grey. At this resolution, the internal structure of the kaolin matrix itself cannot be resolved. Moreover, achieving a spatial resolution of approximately 2 µm requires examination of a very small specimen volume, of the order of 1 cm^3. Figure 3(b) captures the larger pores, predominantly spherical in shape, throughout the entire sample. This highlights the need for the multiscale approach adopted in this study to capture structural complexity within the whole sample.

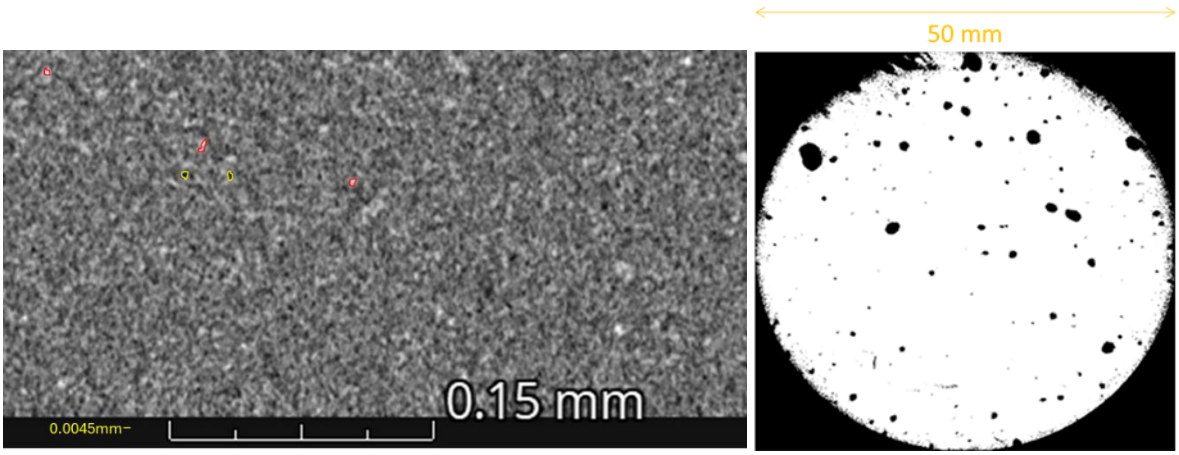

(a) *(b)*

Figure 3. *Horizontal slices of an air-dried kaolin sample preloaded to 50 kPa at (a) higher (2 μm) resolution, showing voids in black, silt particles in white, and the kaolin matrix in grey, and (b) lower (20 μm) resolution, showing large voids in black*

Evaluation of pore space occupied by large pores

Size and volume of pores is quantified for a series of preloading stresses to evaluate the evolution of pore space under increasing load one-dimensionally for i) saturated kaolin samples and ii) air dried kaolin samples.

Porosity is one of the most fundamental parameters used to characterize soil fabric, representing the fraction of the total specimen volume occupied by pore space. It is calculated directly from the segmented 3D image as the ratio of pore-space voxels to the total number of voxels within the specimen volume.

The analysis focuses on the larger pores, hereafter referred to as 'bubbles' for simplicity owing to their predominantly spherical shape. Bubbles larger than approximately 50μm were consistently observed at resolutions of 5μm and 10μm, suggesting that approximately 50μm represents a lower characteristic size for the bubbles present within the kaolin matrix, rather than a resolution-dependent detection limit.

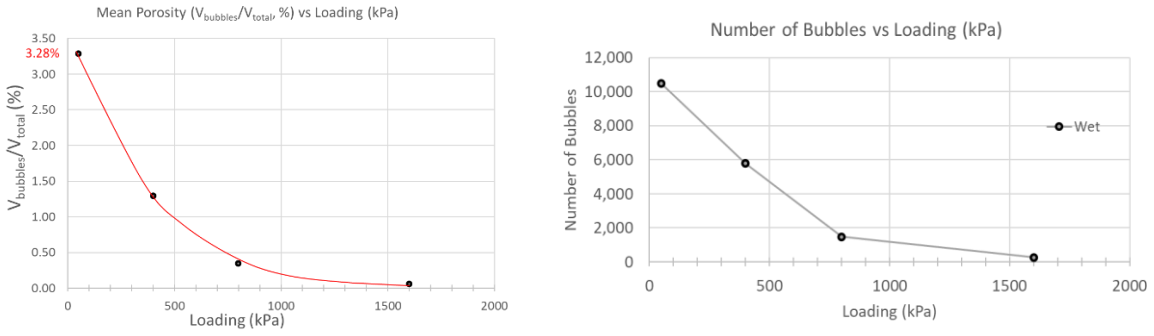

(a) *(b)*

Figure 4. *Quantification of macro-porosity features: (a) volume of bubbles; (b) number of bubbles in wet samples*

Figure 4(a) shows the mean macro-porosity measured at different preloading stresses. The saturated samples, hereafter referred to as 'wet', exhibit a marked reduction in macro-porosity with increasing preload. The results further indicate that the preload-induced structure is largely retained following unloading prior to scanning. This behaviour is attributed to the development of negative pore-water pressure (suction), which maintains effective stress and thereby limits subsequent changes in the preload-induced structure. For example, during drained one dimensional loading to σ_v=400kPa, u=0kPa and, according to Terzaghi's effective-stress principle, $\sigma_v'=\sigma_v-u=400$kPa. Following removal from the oedometer, the externally applied total stress becomes zero. If a pore water pressure of u≈−400kPa is retained, the corresponding effective stress remains approximately 400kPa, thereby preserving the preload-induced structure.

However, the reduction in volume observed in Figure 4(a) is not a uniform process i.e. all bubbles reduce in volume. In Figure 4(b) the number of all bubbles has been counted with increasing preload and it shows that bubbles not only reduce in volume but also in number with loading, indicating that bubbles also collapse. The influence of bubble size on the propensity for collapse will be investigated in the next section.

Having quantified the volume and number of bubbles after reconstitution the effect of drying on the volume and size of the bubbles can be assessed. In Figure 5 the samples allowed to air-dry after unloading are shown in orange. Drying the samples after preloading significantly increases the volume of bubbles compared to the saturated state shown in black, due to air intrusion at pore space. The increase diminishes at the largest preloading.

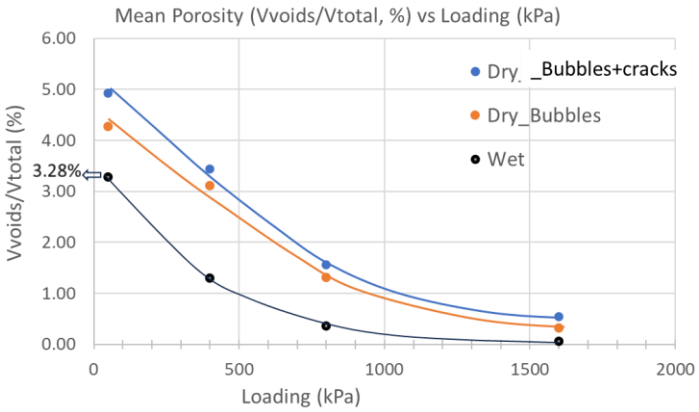

Figure 5. *Quantification of macro-porosity features following air-drying at various preloading stresses*

Considering the full range of preloading stresses, the progressive decrease in the volume of dry bubbles observed in the air-dried specimens appears to reflect the increasingly dense structure induced by one-dimensional loading in the wet state, with this preloading effect remaining evident after air-drying. Also note that the very low measured porosity values (<3.28% for the wet samples) reflect detectable porosity at 20 μm voxel size. The true total porosity of the samples is higher because sub resolution pores, i.e. pores within the kaolin matrix, cannot be imaged at this voxel size. However, since pores larger than approximately 20 μm have been quantified throughout the entire sample, and the total pore volume is independently known from bulk laboratory measurements, the contribution of these macropores to the overall pore space can be assessed. This allows the volume of CT-resolved macropores to be expressed as a fraction of the total pore volume. For example, at a preload of 50 kPa, the total pore volume corresponds to approximately 52% of the specimen volume, whereas the CT-resolved bubble volume represents 3.28%. The bubbles therefore account for approximately 6.3% of the total pore space in the wet sample. Following air-drying, their contribution increases to around 10% of the total pore space.

Air-drying also induces desiccation cracking, and the corresponding crack volume and its evolution with preloading are shown by the blue curve in Figure 5. The crack volume is relatively small compared with the bubble volume. The increase is most pronounced at a preload of 50 kPa, while at higher preloads the crack volume remains comparatively low and shows only limited dependence on preloading. At 1600 kPa, very few cracks are observed, consistent with the very dense structure and the similarly small number of bubbles remaining at this preload.

Evaluation of large Pores Size Distribution (PSD)

Following the labelling of individual pores, the size of every individual pore was calculated to build the pore size distribution (PSD) which shows how many large pores exist at each size and what fraction of the total pore space they occupy.

The equivalent diameter of each pore was calculated from its volume by assuming the pore is a perfect sphere of equal volume:

$$d_{eq} = 2\left(\frac{3V}{4\pi}\right)^{\frac{1}{3}} \qquad (1)$$

where V is the bubble volume in μm³ and d_{eq} is the equivalent spherical diameter in μm.

The cumulative pore size distribution (PSD) was subsequently calculated using the granulometric method (2), implemented in Python via the SPAM library:

$$PSD(r) = \frac{V_{(r)}}{V_{(t)}} \times 100\% \qquad (2)$$

where $V_{(r)}$ is the volume of large-pores space (bubbles) that can accommodate a sphere of radius r, and $V_{(t)}$ is the total bubble volume.

The resulting cumulative distribution is plotted as cumulative pore-volume percentage against equivalent bubble diameter, from which characteristic diameters are determined: D50 is the median equivalent diameter, below which 50% of the total bubble volume is contained, providing a representative measure of the overall bubble-size distribution; and D90 is the equivalent diameter below which 90% of the total bubble volume is contained, characterising the coarser end of the distribution.

Figure 6 shows the PSD curves for the wet samples for a range of applied preloads between 50 kPa to 1600 kPa. A consistent shift of the curves towards smaller pore diameters is observed with increasing preload, indicating progressive closure of pores across the entire size range, in other words, a greater proportion of the surviving pores fall in smaller size classes with increasing load. However, pore closure is more pronounced for the larger pores, as indicated by the relatively small change in D50 compared with the more substantial reduction in D90 in the PSD curves. Together with the decrease in the number of large pores with increasing preload observed in Figure 4(b), this suggests that a significant proportion of the larger pores collapse during the overall volume-reduction process.

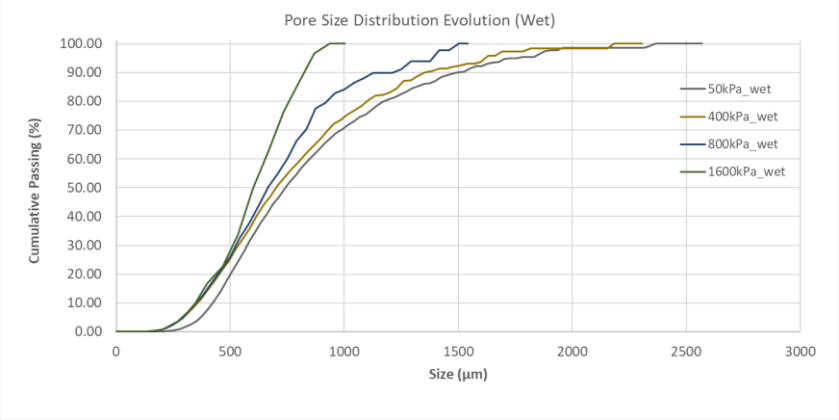

Figure 6. *Evolution of the pore size distribution with increasing preload for wet samples*

Figure 7 presents the pore-size distribution curves after air-drying. Interestingly, the smaller pores, with equivalent diameters below approximately 600 µm, show only limited change; for example, D_{30} remains similar in the wet and dry samples. In contrast, the larger pores increase substantially in size after drying. This is reflected by the flattening of the cumulative distribution curves between D_{50} and D_{90}, indicating a broadening towards larger pore sizes for all preloading levels. Thus, air-drying appears to preferentially enlarge the larger pores, while having comparatively little effect on the smaller ones. Only a small number of pores larger than approximately 2000 µm are observed after drying. This suggests the existence of an upper characteristic size controlling bubble expansion, analogous to the lower characteristic size of approximately 50 µm discussed previously.

Regarding the pore-size distribution, a limiting state appears to be reached at preloads of 400 and 800 kPa. The bubble-size distribution at 50 kPa forms a slightly lower bound, whereas only preloading to 1600 kPa results in a marked reduction in bubble size, reflecting the very dense structure developed under one-dimensional compression. It should be emphasised that the PSD curves characterise the distribution of bubble sizes and do not directly represent bubble volume. In contrast, the total bubble volume decreases monotonically with increasing preload, as shown in Figure 5.

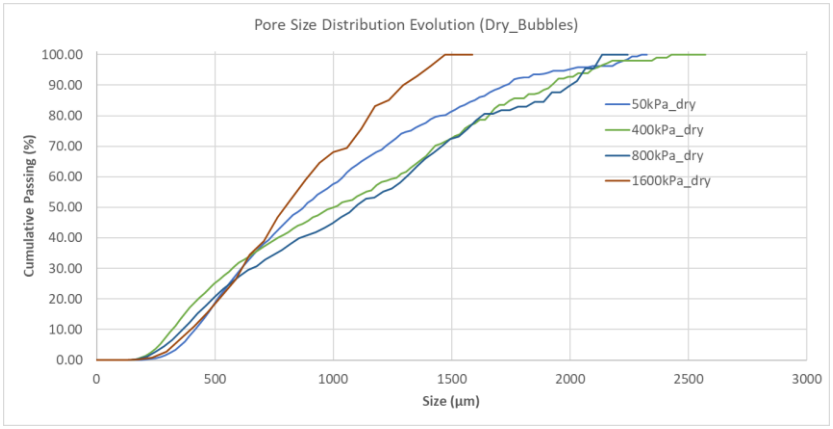

Figure 7. *Evolution of the pore size distribution with increasing preload for dry samples*

A direct comparison of the wet and dry states at different preloads is presented in Figure 8. Given the dense structure developed after preloading to 1600 kPa, the corresponding curves are omitted for clarity. The smallest increase in bubble size upon air-drying is observed for the specimen preloaded to 50 kPa, consistent with the relatively large bubbles already present in this wet state. In contrast, increasing preload progressively reduces both bubble size and number in all wet states (Figure 4). Upon subsequent air-drying, both increase again, reaching sizes that exceed those observed in the dry specimen subjected to the initial preload of 50 kPa. This suggests that the sequence of compression-induced bubble contraction followed by drying-induced expansion influences the final macropore structure.

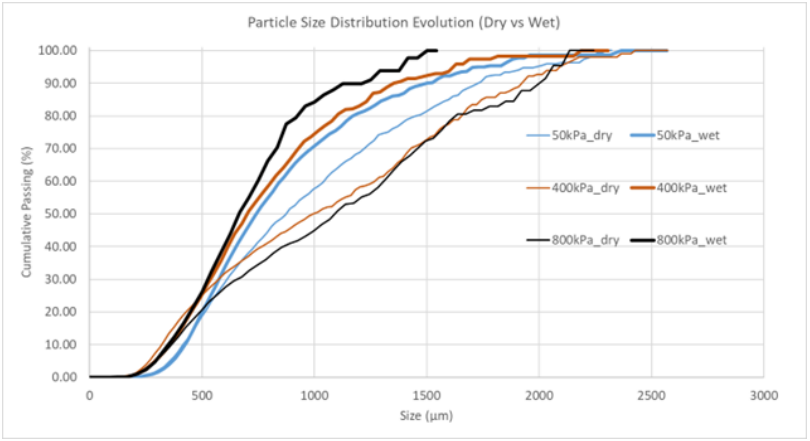

Figure 8. *Comparison of pore size distribution (PSD) curves between wet and air-dried samples at different preloading stresses*

Evolution of total pore space

Since the entire specimen was scanned, changes in total sample volume can be determined directly from the 3D reconstructions. Figure 9(a) presents the settlement developed during one-dimensional loading, calculated from the average of six height measurements, for wet specimens subjected to preloads ranging from 50 to 1600 kPa. The specimen height decreases with increasing preload as the larger pores progressively reduce in volume, as discussed previously (Figure 4), while water is expelled from the specimen. At the same time, compression of the finer, sub-resolution pore network within the kaolin matrix also contributes to the overall volume reduction. The contribution of this finer-scale porosity could therefore be inferred by comparing the total specimen volume change with the change in volume of the larger CT-resolved pores obtained from the 3D reconstructions but is beyond the scope of this paper.

Figure 9(b) shows the evolution of the total volume of the air-dried samples with increasing preload. A trend similar to that observed for the wet specimens is evident, with total sample volume decreasing as preload increases. For a given preload, the dry specimens exhibit greater settlement than the corresponding wet specimens, indicating additional shrinkage during air-drying. Since the larger

pores/bubbles increase in volume and desiccation cracks develop during drying, the overall reduction in sample volume must be primarily associated with contraction of the finer, sub-resolution pore network within the kaolin matrix. This matrix-scale contraction more than compensates for the increase in volume of the larger pores and cracks, which together account for only approximately 10% of the total pore space at 50kPa preload (Figure 5).

Figure 9 qualitatively illustrates the reduction in both the volume and number of large pores with increasing preload. Air-drying leads to enlargement of the volume and number of large pores and the formation of desiccation cracks; however, the overall volume of macro-porosity features still decreases as preload increases.

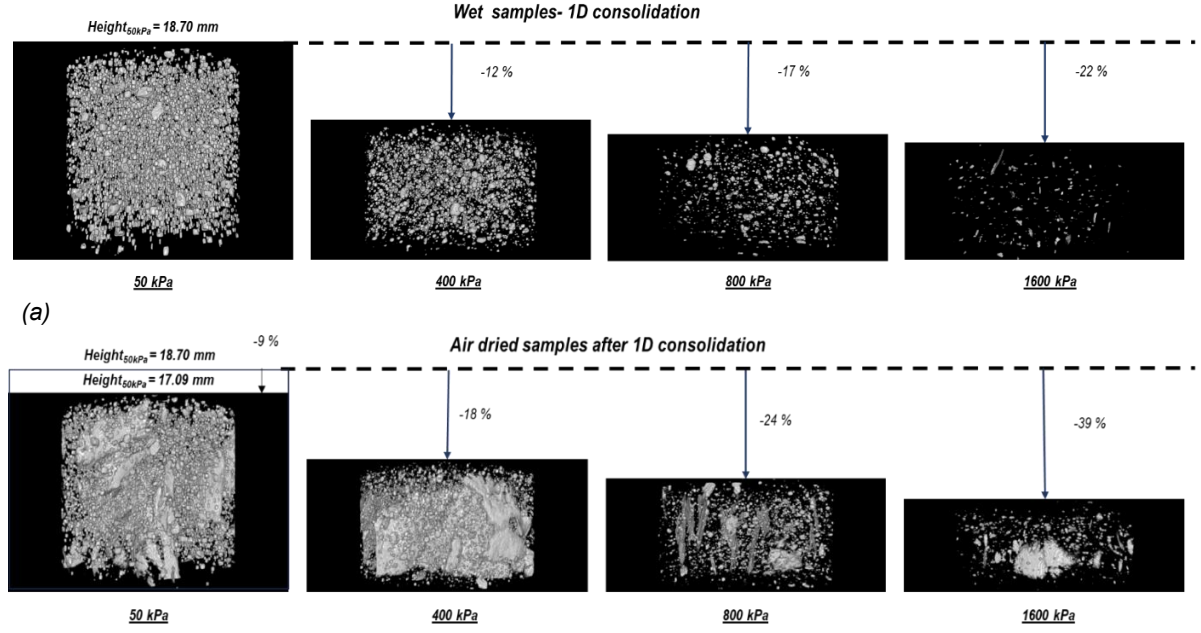

Figure 9. *Volume reduction induced by (a) one-dimensional compression and (b) subsequent air-drying*

CONCLUSIONS

X-ray CT imaging at voxel sizes ranging from 2 to 20 µm was used to investigate the evolution of macro-porosity in reconstituted kaolin during one-dimensional loading and subsequent air-drying. The main conclusions are:

- The reconstituted kaolin contains a distinct population of relatively large, predominantly spherical pores, here termed bubbles, which coexist with the much finer pore network of the clay matrix.
- Under one-dimensional loading in the saturated state, both the size and number of these large pores decrease progressively with increasing preload. The reduction is particularly marked for the larger pores, with macro-porosity becoming negligible at a vertical stress of approximately 1600 kPa.
- The preload-induced reduction in macro-porosity is largely retained after unloading, indicating limited structural recovery and suggesting that the effective stress state is at least partly maintained through the development of suction.
- Air-drying causes the larger pores to increase in size and promotes the formation of desiccation cracks. This effect is most pronounced for the larger pore-size range, whereas the smaller pores show comparatively little change.
- Despite the increase in CT-resolved macro-porosity during drying, the total specimen volume decreases further. This indicates that shrinkage is governed primarily by contraction of the finer, sub-resolution pore network within the kaolin matrix.

- The CT-resolved bubbles and cracks account for only about 10% of the total pore space in the dry state at 50kPa preload. Their enlargement during drying is therefore more than offset by contraction occurring at finer pore scales.
- The results demonstrate that the volumetric response of fine-grained soils cannot be interpreted from a single pore scale alone. Instead, it reflects the coupled evolution of macro-pores, desiccation cracks, and the unresolved pore network within the clay matrix.

REFERENCES

Burland, J. B. (1990). On the compressibility and shear strength of natural clays. Géotechnique, 40(3), 329-378. https://doi.org/10.1680/geot.1990.40.3.329

Casarella, A., Pinzón, G., Sadasivan, V., Stamati, O., Villanova, J., Lukić, B., & Dijkstra, J. (2026). 3D particle aggregation in consolidated clay systems: Insights from phase-contrast nano-holo-tomography. Particuology, 112, 271-283. https://doi.org/10.1016/j.partic.2026.02.002

Desrues, J., Andò, E., Mevoli, F. A., Debove, L., & Viggiani, G. (2018). How does strain localise in standard triaxial tests on sand: Revisiting the mechanism 20 years on. Mechanics Research Communications, 92, 142–146. https://doi.org/10.1016/j.mechrescom.2018.08.007

Finno, R. J., Harris, W. W., Mooney, M. A., & Viggiani, G. (1997). Shear bands in plane strain compression of loose sand. Géotechnique, 47(1), 149–165. https://doi.org/10.1680/geot.1997.47.1.149

Mitchell, J. K. (1976). Fundamentals of soil behavior. John Wiley & Sons.

Myouri, I., Bennai, F., Guyon, J., & Hattab, M. (2025). 3D fabric reconstruction and image processing for clays: New method using SEM-FIB technique and AI. Applied Clay Science, 276, 107943. https://doi.org/10.1016/j.clay.2025.107943

Riedel, I., Andò, E., Salager, S., Bésuelle, P., & Viggiani, G. (2012). Water retention behaviour explored by X-ray CT analysis. In C. Mancuso, C. Jommi, & F. D'Onza (Eds.), Unsaturated soils: Research and applications (pp. 81–88). Springer. https://doi.org/10.1007/978-3-642-31116-1_11

Tchalenko, J. (1967). The influence of shear and consolidation on the microscopic structure of some clays. Ph.D. Thesis, University of London.

Tsantrizou, I. (2025). Laboratory tests on unsaturated soils: oedometer tests, triaxial tests and soil-water retention curves for reconstituted kaolin. Diploma Thesis, NTUA.

Xu, X., Lai, Y., O'Kelly, B. C., & Zhao, B. (2024). 3D deformation and strain fields in drying kaolinite obtained from tracking internal bubbles using X-ray CT and ANN. Acta Geotechnica, 19, 99-113. https://doi.org/10.1007/s11440-023-01948-8

Zhao, B., & Santamarina, J. C. (2020). Desiccation crack formation beneath the surface. Géotechnique, 70(2), 181-186. https://doi.org/10.1680/jgeot.18.T.019

Zheng, Y., & Baudet, B. A. (2025). Pore structure response of reconstituted kaolin and illite-smectite mixed-layer rich clay to 1D compression. Applied Clay Science, 276, 107892. https://doi.org/10.1016/j.clay.2025.107892